Chinese Chemical Letters 34 (2023) 107577

Contents lists available at ScienceDirect

Chinese Chemical Letters

journal homepage: www.elsevier.com/locate/cclet

2D graphene oxide-L-arginine-soybean lecithin nanogenerator for synergistic photothermal and NO gas therapy

Haina Tian[a,b], Jinyan Lin[c], Fukai Zhu[d], Jiaqi Li[b,e], Suhua Jiang[d], Liya Xie[f,*], Yang Li[b,*], Peiyuan Wang[b,*], Zhenqing Hou[a,*], Jinxiao Mi[g]

[a] Department of Biomaterials, College of Materials, Research Center of Biomedical Engineering of Xiamen & Key Laboratory of Biomedical Engineering of Fujian Province, Xiamen University, Xiamen 361005, China
[b] Key Laboratory of Design and Assembly of Functional Nanostructures, Fujian Institute of Research on the Structure of Matter, Chinese Academy of Sciences, Fuzhou 350002, China
[c] The United Innovation of Mengchao Hepatobiliary Technology Key Laboratory of Fujian Province, Mengchao Hepatobiliary Hospital of Fujian Medical University, Fuzhou 350025, China
[d] Collaborative Innovation Center of Mushroom Health Industry, Minnan Normal University, Zhangzhou 363000, China
[e] School of Rare earths, University of Science and Technology of China, Hefei 230026, China
[f] The First Affiliated Hospital of Xiamen University, Xiamen 361003, China
[g] Department of Materials Science and Engineering, Fujian Provincial Key Laboratory of Advanced Materials (Xiamen University), College of Materials, Xiamen University, Xiamen 361005, China

ARTICLE INFO

Article history:
Received 10 March 2022
Revised 31 May 2022
Accepted 31 May 2022
Available online 3 June 2022

Keywords:
NO gas therapy
Photothermal therapy
L-Arg
Immune activation
Reduce recurrence

ABSTRACT

Nitric oxide (NO) gas therapy has been regarded as a promising strategy for cancer treatment. However, its therapeutic efficiency is still unsatisfying due to the limitations of monotherapy. Previous preclinical and clinical studies have shown that combination therapy could significantly enhance therapeutic efficiency. Herein, a graphene oxide (GO)-L-arginine (L-Arg, a natural NO donor) hybrid nanogenerator is developed followed by surface functionalization of soybean lecithin (SL) for synergistic enhancement of cancer treatment through photothermal and gas therapy. The resultant GO-Arg-SL nanogenerator not only exhibited good biocompatibility and excellent endocytosis ability, but also exhibited excellent photothermal conversion capability and high sensitivity to release NO within tumor microenvironment *via* inducible NO synthase (iNOS) catalyzation. Moreover, the produced hyperthermia and intracellular NO could synergistically kill cancer cells both *in vitro* and *in vivo*. More importantly, this nanogenerator can efficiently eliminate tumor while inhibiting the tumor recurrence because of the immunogenic cell death (ICD) elicited by NIR laser-triggered hyperthermia and the immune response activation by massive NO generation. We envision that the GO-Arg-SL nanogenerator could provide a potential strategy for synergistic photothermal and gas therapy.

Recently, owing to the "green" treatment paradigm with ignorable side effects, gas therapy (GT) has drawn wide attention from scientists [1–4]. Some gaseous transmitters, like NO (nitric oxide) [5,6], CO (carbon monoxide) [7,8], and H_2S (hydrogen sulfide) [9–11] have been demonstrated to interfere with the pathophysiological and physiological processes [12–14]. Among these gasses, nitric oxide (NO) acts as a critical bioregulator, involved in modulating blood vessels, neurotransmission, system infection of the immune response, and other intracellular activities [15–19]. Motivated by the versatile bio-functions, extensive efforts have been made to explore the potential therapeutic agents, especially in the field of tumor ablation. Therefore, numerous researches proved that NO is capable of serving as a tumor inhibitor, including cell cycle arrest and cellular apoptosis stimulation *via* various mechanisms, such as cytotoxic substance (like ONOO-) formation [20–24], protein nitrification [25], cytochrome C generation [26], and mitochondrial permeability increase [27]. However, the short half-life and random diffusion properties substantially impend its clinical application [28]. To achieve spatial and temporal controlled NO release in desirable sites, continuous efforts in NO donors have been intensively exploited. Nevertheless, a large amount of NO donors, like BNN6 and *N*-nitrosamines, often produce undesirable by-products that could in turn induce tumor [29,30]. Fortunately, L-arginine (L-Arg), a natural NO donor presents superior biocompatibility and

* Corresponding authors.
E-mail addresses: xly885@163.com (L. Xie), li.yang@fjirsm.ac.cn (Y. Li), wangpeiyuan@fjirsm.ac.cn (P. Wang), houzhenqing@xmu.edu.cn (Z. Hou).

https://doi.org/10.1016/j.cclet.2022.05.091
1001-8417/

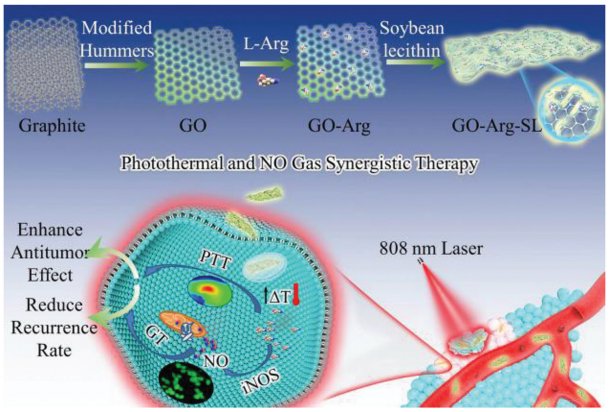

Scheme 1. Schematic illustration of stepwise GO-Arg-SL fabrication for synergistic antitumor effect of photothermal therapy and gas therapy.

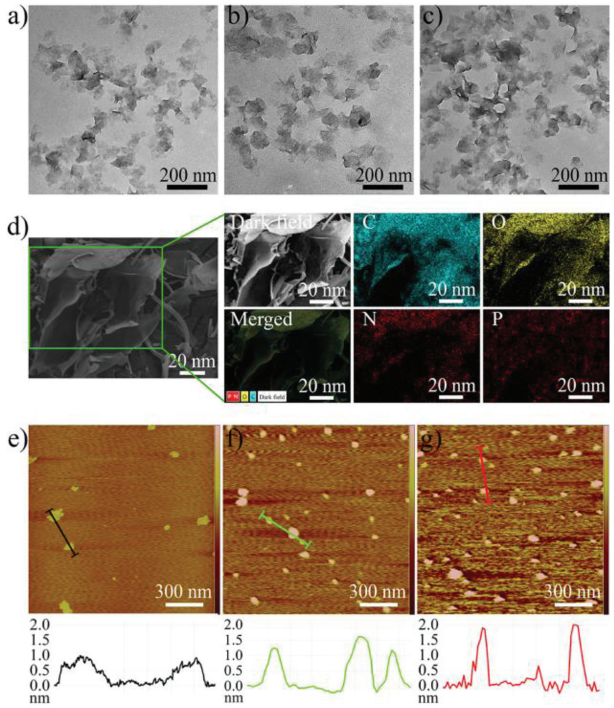

Fig. 1. TEM images of (a) GO, (b) GO-Arg and (c) GO-Arg-SL. (d) SEM, element mapping and merged images of GO-Arg-SL by EDS analysis. Representative AFM images and height profiles of (e) GO, (f) GO-Arg and (g) GO-Arg-SL based on AFM analysis.

could release NO under inducible NO synthase (iNOS) or ROS (reactive oxygen species) catalyzation. Accordingly, it's urgent to explore an ideal delivery platform to realize the precise and effective NO generation in tumor cells [31,32].

Among the drug delivery platforms, graphene-based nanomaterials (like graphene oxide, GO) have been explored as a brilliant system owing to the 2D planar nanostructure, large specific surface area, and various functional groups on the surface [33,34]. Simultaneously, GO exerts diverse utilization in bio-imaging, bio-sensing, and photothermal therapy. In which, photothermal therapy (PTT) of GO is featured with non-invasive capability, high thermal conversion efficiency, and low systemic side effects [35–37]. However, hyperthermia-induced by near-infrared region light (NIR, 808 nm) usually leads to upregulating the expression of the heat shock protein, thereby resulting in the heat stress tolerance of tumor cells and decreasing the therapeutic effects of PTT [38]. Therefore, it is satisfactory to design a multi-functional nanosystem to rationally combine other tumor therapy modulations with PTT for overcoming the limitations of single PTT *via* a fascinating synergistic treatment [39]. In view of the above investigation, the GO-based L-Arg delivery nanoplatform candidate could be expected to synergistically combine GT with PTT to realize an ideal antitumor effect.

Herein, we have successfully fabricated GO nanomaterials *via* a modified Hummers' strategy. Then, the formed carboxyl group on GO surface and large specific surface area facilitate L-Arg loading (GO-Arg). Lastly, the surface of GO-Arg nanogenerator was then functionalized with soybean lecithin (SL) to improve its hydrophilic capability and biocompatibility (Scheme 1). After intravenous injection into 4T1 breast tumor-bearing mice, the resultant GO-Arg-SL nanogenerator could be effectively accumulated at the tumor sites by EPR (enhanced permeability and retention) effect and then efficiently internalized by tumor cells. Moreover, L-Arg could be efficaciously released in the cytoplasm of tumor cells then it was catalyzed by iNOS to generate massive NO for GT. Meanwhile, GO nanomaterial can act as a photothermal agent for hyperthermia generation. Therefore, tumors were remarkably eliminated attributed to the enhanced antitumor effect of PTT and GT. More importantly, this nanogenerator can efficiently cut down on the tumor recurrence rate due to the ICD (immunogenic cell death) induced by NIR laser-triggered hyperthermia and the immune activation by abundant NO generation [40]. This synergistic therapy of our GO-Arg-SL nanogenerator holds great potential for eradicating malignant tumors in clinical.

In this work, the size and morphology of as-prepared nanoparticles were characterized. Fig. 1a showed the thin sheets of GO with a size of ~120 nm as determined by transmission electron microscopy (TEM). Moreover, according to the atomic force microscopy (AFM) image, the thickness of GO nanomaterial was analyzed as ~1.0 nm (Fig. 1e). After L-Arg-loaded on the GO surface *via* electrostatic interaction, the sheet-like morphology of GO-Arg was maintained (Fig. 1b), but the thickness of GO-Arg slightly increased to ~1.3 nm (Fig. 1f), demonstrating the integration of L-Arg and GO nanomaterial was successful. Subsequently, SL was modified on the surface of GO-Arg (GO-Arg-SL) by a thin-film strategy in order to prevent serious premature L-Arg leakage, improve biocompatibility and long blood circulation [41]. TEM and AFM images showed GO-Arg-SL with lamellar nanostructure was similar to GO and GO-Arg (Figs. 1c and g), and the thickness was a bit increase, demonstrating that SL modification only caused an insignificant change in GO morphology. Meanwhile, ultra-thin and monodisperse nanomaterials were further demonstrated as shown in Fig. S1 (Supporting information). Scanning electronic microscopy (SEM) images also revealed that GO-Arg-SL has consisted of randomly stacked nanosheets (Fig. 1d). Then element mapping was performed by energy-dispersive X-ray spectroscopy (EDS) analysis to obtain more insight into the distribution of the elements in our GO-based nanosystem. Excitedly, C, O, N and P were found to be dispersed all over the GO surface (Fig. 1d, Fig. S2 and Table S1 in Supporting information). C and O could be primarily derived from the GO, N and P originated from L-Arg and SL, respectively. In addition, substantial improvement of dispersibility and stability can be observed in GO-Arg-SL, attributing to the effective modification of SL (Fig. S3 in Supporting information). All results confirmed the successful construction and homogeneous composition of GO-Arg-SL.

Then, the physical and chemical structure of the as-synthesized nanomaterials was further investigated. Fig. 2a exhibited that GO-Arg-SL appeared maximum absorption peaks at 202 nm and 230 nm, which were assigned to the characteristic peaks of L-Arg and C=O in GO, respectively. As shown in Fig. 2b, compared to the absorption peaks of GO, a new peak at 1553 cm^{-1} was detected in GO-Arg which attributed to the stretching vibration peak of

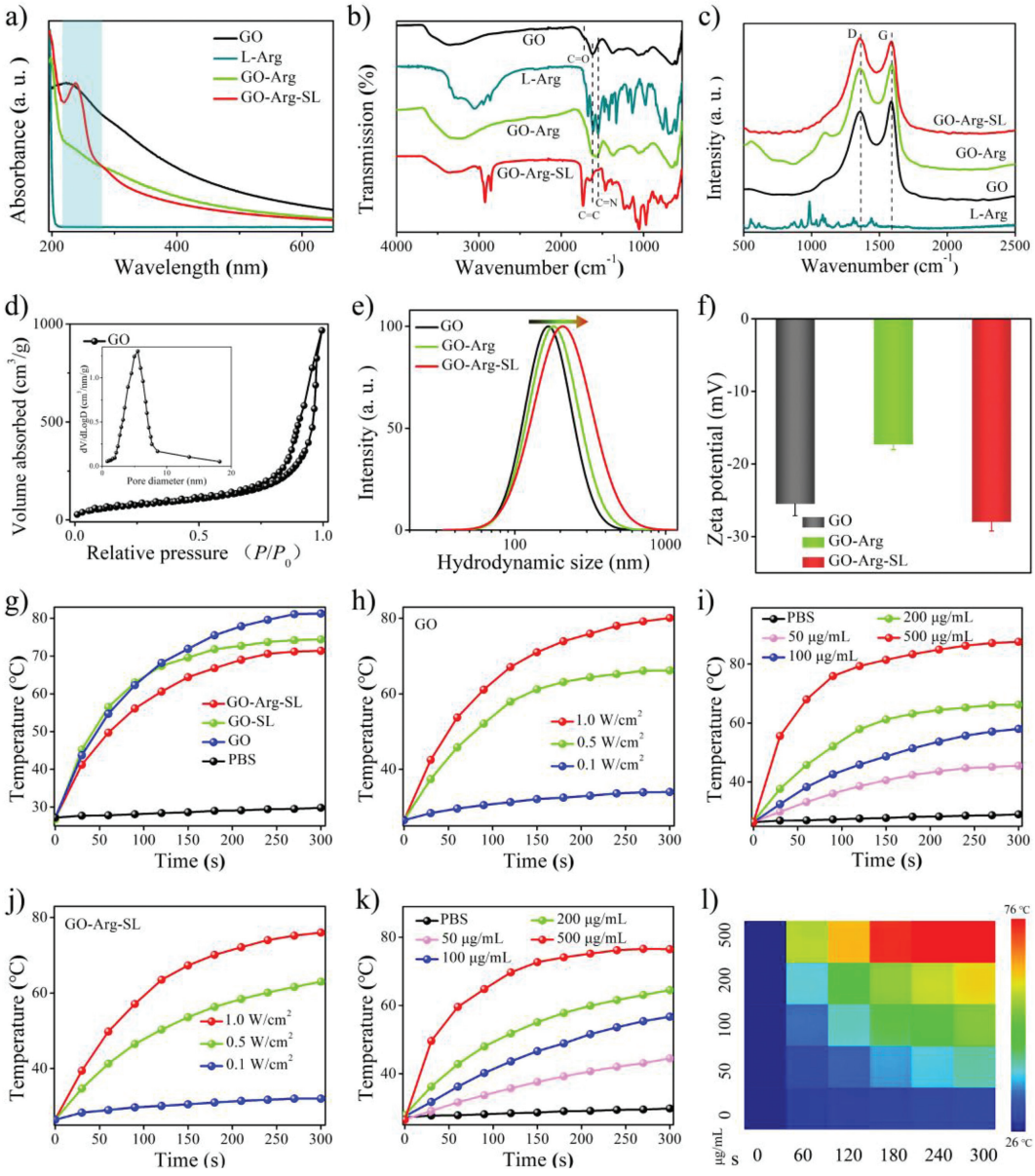

Fig. 2. (a) UV-vis, (b) FTIR and (c) Raman spectra of GO, L-Arg, GO-Arg and GO-Arg-SL. (d) Nitrogen adsorption-desorption and pore size distribution of GO. (e) Size distribution and (f) zeta potential of GO, GO-Arg, and GO-Arg-SL. (g) Photothermal curve of different formulations with 808 nm laser irradiation. Temperature curve of (h) GO and (j) GO-Arg-SL under 808 nm laser irradiation with different power density. (i) Temperature curve of GO with different concentrations under 808 nm laser irradiation for various times. (k) Temperature curve and (l) photothermal images of GO-Arg-SL with different concentrations under 808 nm laser irradiation for various times.

-C=N- in L-Arg. Interestingly, the above characteristic peaks of both -C=C- and -C=N- almost disappeared in GO-Arg-SL, approving the successful coating of SL. Moreover, the Raman spectrum was often used to distinguish the crystal performance of carbon-based nanomaterials. The manifested D band (1343 cm^{-1}) and G band (1584 cm^{-1}) can be observed in GO, GO-Arg, and GO-Arg-SL, verifying the existence of GO nanomaterials. Importantly, in comparison with the intensity ratio of I_D/I_G band of GO (0.96), that of GO-Arg-SL obviously increased to 1.03, demonstrating that the modification of L-Arg and SL has influenced the surface of graphene sheets. In short, the Raman spectra further proved the successful modification of L-Arg and SL (Fig. 2c). Immediately, the specific surface area of GO nanomaterial was determined by a conventional nitrogen adsorption/desorption method and further calculated by a model of Brunauer Emmet Teller (BET). As shown in Fig. 2d, our as-prepared GO nanomaterial presented a specific surface area of ~364.9 m^2/g with the pore diameter of ~5.5 nm which facilitates a large amount of L-Arg loading. We then investigated the size distribution of GO-Arg-SL by dynamic laser scanning. As displayed in Fig. 2e, the size of GO-based nanomaterials gradually increased from 176 nm to 195 nm, further proving the reliability of our approach for L-Arg loading and SL modification. Simultaneously, after L-Arg loading, zeta potential significantly decreased owing to charge neutralization between $-NH_2$ in L-Arg and -COOH in GO. In addition, the negative charge of GO-Arg-SL increased again, resulting from phosphate groups in SL (Fig. 2f). *In vitro* hemolysis assay was explored after SL coating of GO-Arg, fortunately, no hemolytic effects occurred even in presence of 200 μg/mL GO-Arg-SL nanomaterials, proving the enhanced hemocompatibility of SL modification (Fig. S4 in Supporting information). Meanwhile, *in vitro* photothermal evaluation of the nanomaterials under an 808 nm laser irradiation was investigated by IR camera. Fig. 2g showed the temperature of GO (400 μg/mL) reached about 80 °C within 300 s, meanwhile, that of GO-Arg-SL with the

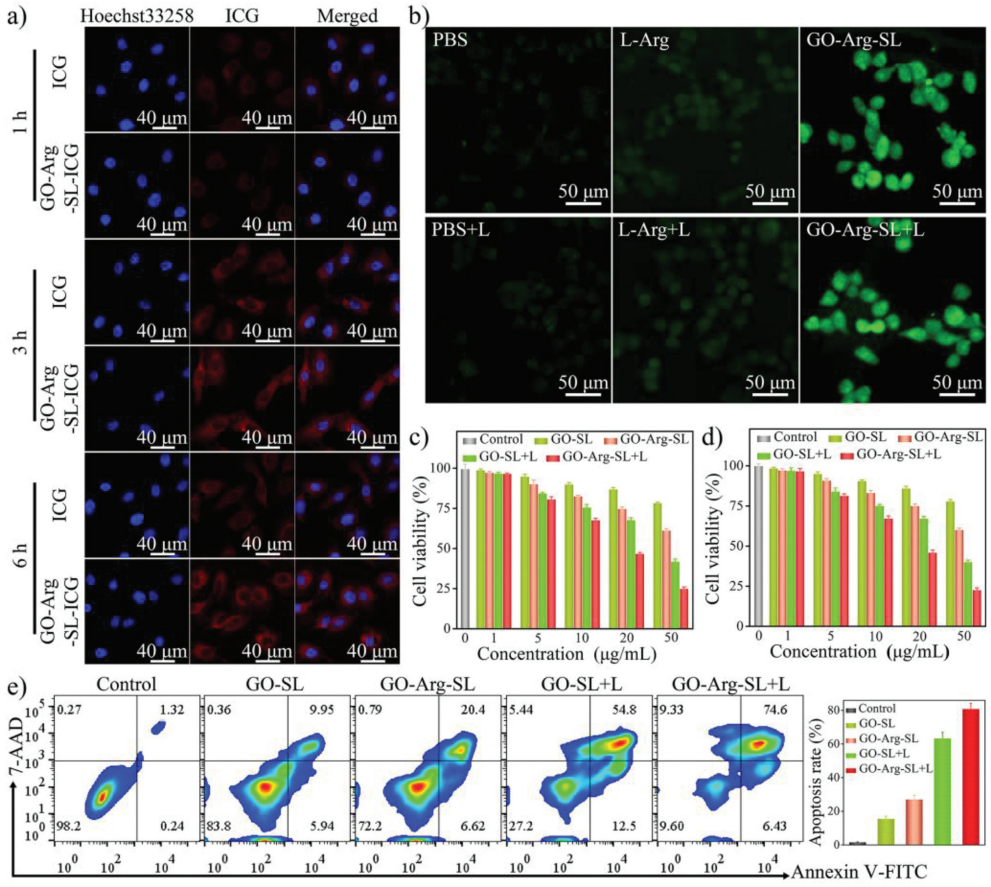

Fig. 3. (a) CLSM images of 4T1 cells after incubation with GO-Arg-SL-ICG and ICG for different time. Scale bars: 40 μm. (b) CLSM images of intracellular NO in groups of PBS, free L-Arg, GO-Arg-SL without and with 808 nm laser irradiation, respectively. Scale bars: 50 μm. Cell viability of (c) 4T1 cells and (d) A549 cells after PBS (control), GO-SL, GO-Arg-SL, GO-SL+L and GO-Arg-SL+L treatments under various concentrations. (e) Flow cytometry studies and quantitative analysis of PBS+L (control), GO-SL, GO-Arg-SL, GO-SL+L and GO-Arg-SL+L induced apoptosis/necrosis in 4T1 cells.

same concentration exhibited similar photothermal performance with a slight high temperature reduced (68 °C). This is mainly due to L-Arg conjugation and SL modification. In sharp contrast, the temperature of the PBS group had ignorable fluctuation, demonstrating a high thermal conversion efficiency of GO and GO-Arg-SL (Figs. 2g–l). Meanwhile, the concentration-dependent photothermal property was found from the infrared thermal images (Figs. 2i, k, and l). We could intuitively observe that the temperature was positively correlated with GO concentration, furthermore, GO-Arg-SL evinced photothermal stability even after four cycles of 808 nm NIR irradiation (Fig. S5 in Supporting information), suggesting that our GO-Arg-SL was an ideal photothermal agent for tumor cell ablation.

Effective cellular internalization plays a vital role in drug delivery. To estimate the cellular internalization efficiency, indocyanine green (ICG), as a fluorescent probe, labeled GO-Arg-SL (GO-Arg-SL-ICG) through the π-π stacking interaction. As displayed in Fig. 3a of confocal laser scanning microscope (CLSM) images, comparative cells exerted red fluorescence and no signals presented in nuclei with both ICG and GO-Arg-SL-ICG incubation for 1 h or 3 h, proving the effective endocytosis capability of tumor cells under GO-Arg-SL-ICG co-incubated condition. Interestingly, after 6 h co-culture, the red fluorescence in the free ICG group became weaker and fluorescent intensity was obviously lower than that of GO-Arg-SL-ICG treatment. This might be attributed to the relatively high drug delivery and low exocytosis capacity of GO-based nanocarrier in comparison with free drugs. Subsequently, we evaluated consecutive NO generation in the cytoplasm with a typical NO indicator, DAF-FM DA probe. To directly demonstrate the NO generation from L-Arg, a series of tumor cell groups were set including PBS, free L-Arg, and GO-Arg-SL groups without and with an 808 nm laser irradiation. As expected, a considerable amount of NO generation was found in GO-Arg-SL and GO-Arg-SL+L groups which exhibited the strongest fluorescence compared with other groups regardless of light variations, while only weak NO was generated in the L-Arg group owing to the finite free L-Arg entered into tumor cells (Fig. 3b). In addition, cytoplasm NO generation was also investigated thoroughly by flow cytometry that NO amount in GO-Arg-SL and GO-Arg-SL+L was exceedingly higher than other four groups (Fig. S6 in Supporting information), further demonstrating GO-based nanocarrier was suitable for L-Arg delivery. Subsequently, CCK-8 assay and living/dead staining were used to evaluate the cytotoxicity of nanoparticles. Obviously, the cytotoxicity of GO-Arg-SL+L was much stronger than that of other groups (Figs. 3c and d, Figs. S7 and S8 in Supporting information), revealing the synergistic effect of GT and PTT. Besides, the tumor cells inhibition ability of L-Arg loaded GO-based nanocarrier was further detected by flow cytometry. Undoubtedly, GO-Arg-SL with an 808 nm laser had the best ability to induce tumor cell apoptosis compared with other groups (Fig. 3e), which was identical to the above results of cell viability and living/dead cell staining.

Inspired by *in vitro* cellular internalization results of GO-Arg-SL, we then examined the tumor accumulation capacity and biodistribution of GO-Arg-SL in BALB/c mouse with 4T1 breast tumor.

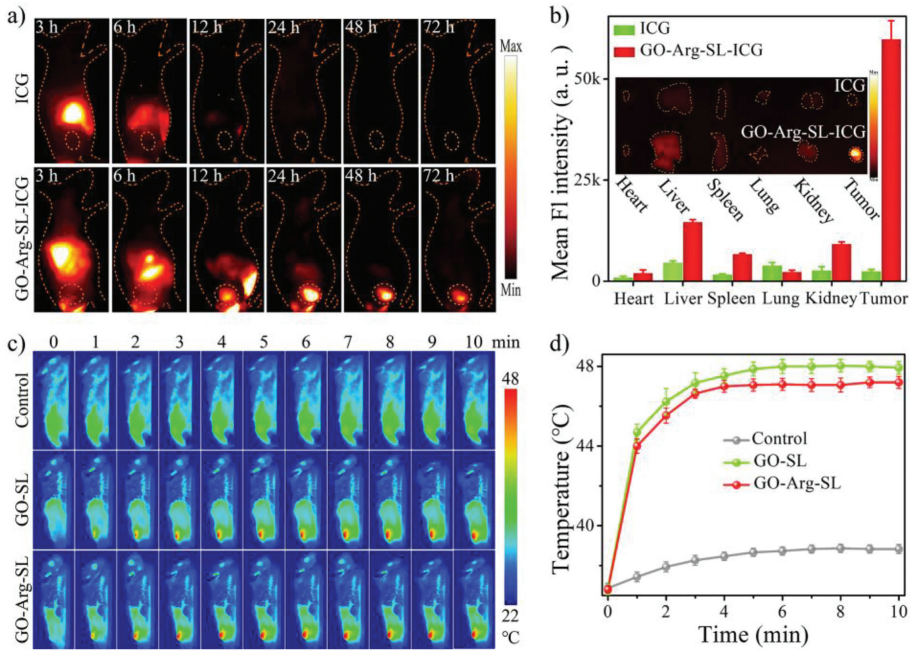

Fig. 4. (a) NIR-II fluorescence images of tumor-bearing BALB/c mouse after intravenous injection of ICG and GO-Arg-SL-ICG at different time points. (b) The quantitative analysis of NIR-II signal intensity of major organs and tumors in BALB/c mouse after intravenous injection of ICG and GO-Arg-SL-ICG at 24 h. Insert, *ex vivo* NIR-II fluorescent image of major organs and tumors. (c) Photothermal images of BALB/c mouse with 808 nm laser illumination for various times after 24 h intravenous injection of PBS (control), GO-SL and GO-Arg-SL. (d) Reprehensive temperature increase curve of photothermal images in the above three groups.

All animal experiments were conducted in accordance with relevant guidelines approved by the Institutional Animal Care and Use Committee of Xiamen University (Ethics Approval: No. XMU-LAC20180037). Fluorescence imaging is an ideal diagnostic imaging platform to monitor the tumor size and tumor morphology for therapeutical guidance due to the high resolution, noninvasive discrimination between the tumor and normal tissues. We firstly entrapped ICG into GO-Arg-SL (GO-Arg-SL-ICG) to investigate the tumor accumulation behavior with the assistance of NIR-II (second near-infrared region, 900–1700 nm) fluorescence imaging system (1000 nm long pass filter) under an 808 nm laser illumination after intravenous administration *in vivo*. Excitedly, NIR-II fluorescent signal of free ICG group can only be detected after 3–12 h injection in the liver, however, no obvious fluorescence signal was detected at the tumor during the whole procedure (Fig. 4a). This result should be attributed to the rapid clearance and low blood retention properties of free ICG. Contrarily, it presented that the NIR-II fluorescent signal of GO-Arg-SL-ICG treatment in tumor site substantially enhanced from 12 h post-injection. The maximum tumor accumulation of GO-Arg-SL-ICG was found after intravenous injection at 24 h, demonstrating the effectively active tumor accumulation ability of GO-based nanoparticles (Fig. 4a and Fig. S9 in Supporting information). Compared with free ICG group, *ex vivo* NIR-II fluorescent images of major organs and tumors exhibited that the fluorescence intensity of the GO-Arg-SL-ICG group was the strongest intensity at tumor site which are consistent with cellular internalization data (Fig. 4b). Motivated by maximum accumulation value at tumor site after 24 h injection, subsequently, *in vivo* hyperthermic performance induced by NIR laser irradiation was carried out at this time point. Photothermal images of control, GO-SL, GO-Arg-SL treatment with continuous 808 nm laser (0.5 W/cm^2) were obtained *via* IR thermal camera. The control group with PBS administration only presented negligible temperature rose, comparatively, the local temperature in GO-SL, GO-Arg-SL injection group rapidly climbed to 47.5 °C within 5 min (Figs. 4c and d), further confirming the high photothermal converting capability of GO-based nanomaterials.

Attested by the excellent tumor accumulation of GO-Arg-SL after intravenous administration, we next performed the antitumor effect of GO-Arg-SL *in vivo*. BALB/c mice with subcutaneous 4T1 breast tumor ($n = 5$) have been intravenously vaccinated with PBS+L (control), GO-SL, GO-Arg-SL, GO-SL+L and GO-Arg-SL+L, respectively. All GO-based administration groups had the same equivalent GO-Arg-SL concentration (10 mg/kg). Tumor volume, body weight, and surviving mice were recorded every three days. As shown in Figs. 5a and b, and Fig. S9, in contrast with the control group, the tumor outline and tumor volume in GO-Arg-SL treated mice displayed some extent antitumor effect while still presenting homologous tumor growth trend as GO-SL. Contrarily, GO-SL+L and GO-SL-Arg+L administrated tumors were clearly smaller or totally disappeared with tumor volume significantly reduced (Figs. 5a and b, Fig. S10 in Supporting information). Interestingly, tumor recurrence can be detected after 12 days of treatment in GO-SL+L group, reflecting that even PTT can be an effective local antitumor modality, but it might not completely eradiation all tumor cells, resulting in tumor recurrence or metastasis (Figs. 5a, b and e, and Fig. S10). The above result further proved single PTT or GT was inadequate for effective tumor eradication. Finally, tumor cell apoptosis status was further analyzed by hematoxylin & eosin (H&E) and terminal deoxynucleotidyl transferase dUTP nick end labeling (TUNEL) staining analysis. In contrast, remarkable loosen tumor cells and apoptotic cells were found in GO-SL-Arg+L group with strikingly higher survival rate in comparison with other formulations (Figs. 5d and f). Meanwhile, no body weight variation, little biochemistry fluctuations, and negligible blood routines alternation and pathological changes were found during the whole treated procedure, indicating the biocompatibility and low side effect of the GO-based nanomaterials (Fig. 5c and Figs. S11–S13 in Supporting information). Exactly, 7 days in our work was insufficient for a long-term toxicity evaluation and the systemic toxicity of our GO-Arg-SL with long time durations will be comprehen-

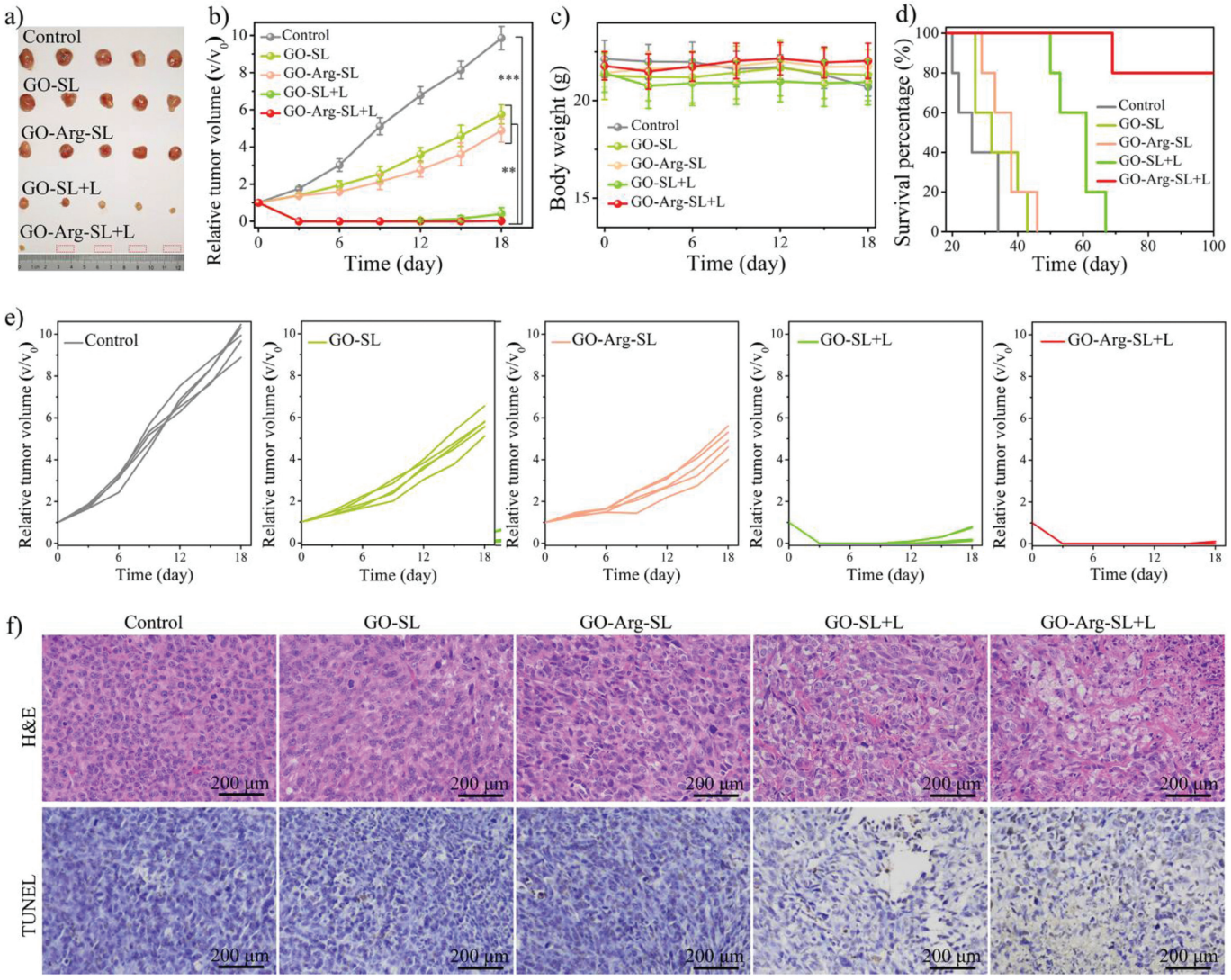

Fig. 5. (a) Photographs of resected tumors after various treatments for 18 days. The red dotted rectangle represented the disappeared tumors. (b) Tumor volume curves, (c) body weights fluctuation, (d) survival rates, (e) tumor volume curves of each mouse with different treatments. (f) H&E and TUNEL staining images of tumor after various treatments for 18 days. $^{***}P < 0.001$ and $^{**}P < 0.01$. Data above are presented as means with standard deviations (mean ± SD, $n = 5$).

sively studied in the future. Collectively, the above results indicated that the combination of PTT and GT of GO-Arg-SL+L with high biosafety may be an effective therapeutic agent that can successfully suppress tumor growth and inhibit malignancy recurrence.

Encourage by the tumor recurrence inhibition ability after GO-Arg-SL+L treatment, we were motivated to explore the underlying mechanism. An emerging area of interest is the activating effect of PTT on the immune system since PTT not only induces tumor cell death but also releases tumor antigens from dying tumor cells, one of the most popular characteristics of ICD [40,42]. The tumor antigens then could be transported into spleen or lymph nodes, then they were expected to stimulate the dendric cells (DCs) homing and maturation which could promote a systemic host immune response [43]. The mature DCs (CD80+/CD86+) was estimated in the tumor draining lymph nodes at day 7 post-treated with various formulations, in addition, the increased DCs percentage was most pronounced in GO-Arg-SL+L administration (16.1%, Figs. 6a and c). In comparison with single PTT of GO-SL+L (11.1%), GO-Arg-SL+L induced more DCs generation, the underlying mechanism was attributed to the immunosuppressive tumor microenvironment reversion effect of massive NO generation [44]. Moreover, the antigen-presenting DCs' maturation activated the innate immunity which can prime cytotoxic T lymphocytes (CTLs) for antitumor immunity [45]. We then evaluated the CTLs content *via* flow cytometry in various formulations. As a consequence, the CD8+CD4−/CD3+ significantly increased in the spleen with GO-Arg-SL+L treatment which was identical to mature DCs percentage, indicating the capability of PTT-induced and gas therapy mediated ICD to elicit an adaptive immune response for further reducing tumor invasion and enhancing anti-tumor immune responses (Figs. 6b and d).

In conclusion, because of the high specific surface area and massive pore in GO, L-Arg was loaded into GO nanomaterials *via* electrostatic interaction. For biocompatibility and adverting L-Arg from leakage, SL was coated on the surface of GO right after L-Arg loading (GO-Arg-SL). Interestingly, ICG labeled GO-Arg-SL presented more valid breast tumor cell uptake in comparison with free ICG *in vitro*. Furthermore, substantial NO generation was found in the cytoplasm after GO-Arg-SL treatment, suggesting that GO-Arg-SL is an optimal gas therapy agent. NIR-II fluorescent imaging results of GO-Arg-SL treated BALB/c mice with subcutaneous breast tumor further proved the effective tumor accumulation capability of GO-Arg-SL. Therefore, breast tumors were totally inhibited *via* gas therapy from L-Arg precise delivery and hyperthermia-induced

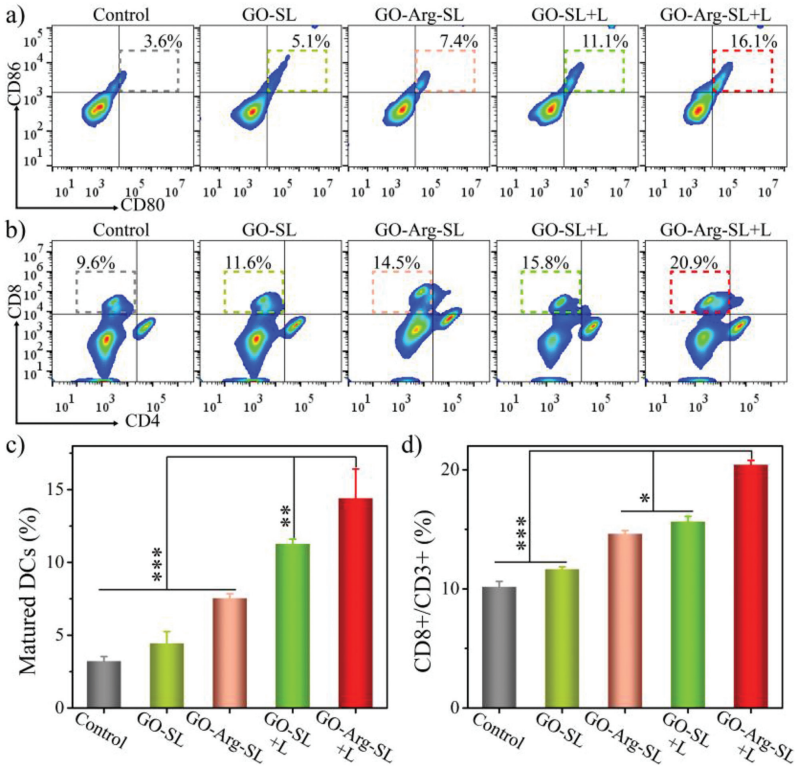

Fig. 6. Flow cytometry analysis of (a, c) mature DCs maturation (CD80+CD86+ gated on CD11c+) in the tumor draining lymph node and (b, d) CTLs (CD8+CD4− gated on CD3+) in the spleen after 7 days treatments of PBS+L (control), GO-SL, GO-Arg-SL, GO-SL+L and GO-Arg-SL+L. $^{***}P < 0.001$, $^{**}P < 0.01$, and $^{*}P < 0.05$. Data above are presented as means with standard deviations (mean ± SD, $n = 4$).

cell death from GO under an 808 nm laser exposure. Furthermore, the above synergistic effect-induced immunotherapy could further inhibit malignancy recurrence. Our GO-based L-Arg delivery nanocarriers are expected to act as a powerful nanoplatform for synergistic eradication of carcinomas in clinical.

Declaration of competing interest

The authors declare that they have no known competing financial interests or personal relationships that could have appeared to influence the work reported in this paper.

Acknowledgments

The authors acknowledge funding from the National Natural Science Foundation of China (Nos. 61905248, 62005284 and 82001950), Natural Science Foundation of Fujian Province of China (No. 2019J01572), China Postdoctoral Science Foundation (No. 2020M671928), Research Start-up Funding of the Mengchao Hepatobiliary Hospital of Fujian Medical University (No. QDZJ-2019-003), and Youth Innovation Foundation of Xiamen City (No. 3502Z20206084).

Supplementary materials

Supplementary material associated with this article can be found, in the online version, at doi:10.1016/j.cclet.2022.05.091.

References

[1] R. Wang, X. Xia, Y. Yang, et al., Adv. Healthc. Mater. 11 (2022) 2102017.
[2] Q. Lu, T. Lu, M. Xu, et al., Biomaterials 257 (2020) 120236.
[3] Y. Qian, J.B. Matson, Adv. Drug Deliv. Rev. 110 (2017) 137–156.
[4] J. Gehring, B. Trepka, N. Klinkenberg, et al., J. Am. Chem. Soc. 138 (2016) 3076–3084.
[5] H.F. Zhou, H.M. Yan, Y. Hu, et al., ACS Nano 8 (2014) 7305–7317.
[6] Y.Y. Huang, J.N. Zhang, Y. Zhang, et al., Mater. Des. 211 (2021) 110160.
[7] D. Zhu, Z. Liu, Y. Li, et al., Biomaterials 274 (2021) 120894.
[8] Q.J. He, D. Kiesewetter, Y. Qu, et al., Adv. Mater. 27 (2015) 6741–6746.
[9] K. Modis, E.M. Bos, E. Calzia, et al., Br. J. Pharmacol. 171 (2014) 2123–2146.
[10] J.M. Kang, Z. Li, C.L. Organ, et al., J. Am. Chem. Soc. 138 (2016) 6336–6339.
[11] B. Liu, S. Liang, Z. Wang, et al., Adv. Mater. 33 (2021) 2101223.
[12] S.W. Ryter, J. Alam, A.M.K. Choi, Physiol. Rev. 86 (2006) 583–650.
[13] P. Pacher, J.S. Beckman, L. Liaudet, Physiol. Rev. 87 (2007) 315–424.
[14] A.R. Butler, D.L.H. Williams, Chem. Soc. Rev. 22 (1993) 233–241.
[15] A. Tiemuer, H. Yu, C. Zhao, et al., Chem. Eng. J. 430 (2022) 132858.
[16] C. Bogdan, Nat. Immunol. 2 (2001) 907–916.
[17] N. Cureton, I. Korotkova, B. Baker, et al., Theranostics 7 (2017) 3715–3731.
[18] Z.J. Huang, J.J. Fu, Y.H. Zhang, et al., J. Med. Chem. 60 (2017) 7617–7635.
[19] Z. Wang, C.Z. Feng, H.J. Zhao, et al., Theranostics 5 (2015) 504–514.
[20] A.E. Maciag, R.J. Holland, Y. Kim, et al., J. Med. Chem. 57 (2014) 2292–2302.
[21] Y. Hu, T. Lv, Y. Ma, et al., Nano Lett. 19 (2019) 2731–2738.
[22] D.A. Wink, J.B. Mitchell, Free Radic. Biol. Med. 25 (1998) 434–456.
[23] D. Fukumura, S. Kashiwagi, R.K. Jain, et al., Nat. Rev. Cancer 6 (2006) 521–534.
[24] D.W. Jiang, T. Yue, G.C. Wang, et al., New J. Chem. 44 (2020) 162–170.
[25] C. Hu, X.L. Cun, S.B. Ruan, et al., Biomaterials 168 (2018) 64–75.
[26] Y. Xu, H. Ren, J.W. Liu, et al., Nanoscale 11 (2019) 5474–5488.
[27] R. Kinoshita, Y. Ishima, M. Ikeda, et al., J. Control. Release 217 (2015) 1–9.
[28] Y. Yang, Z. Huang, L.L. Li, et al., Nanoscale 13 (2021) 444–459.
[29] J. Fan, N. He, Q. He, et al., Nanoscale 7 (2015) 20055–20062.
[30] Y. Yang, Z. Huang, L. Li, Nanoscale 13 (2021) 444–459.
[31] M.M. Wan, H. Chen, Q. Wang, et al., Nat. Commun. 10 (2019) 966.
[32] L. Wang, Y. Chang, Y.L. Feng, et al., Nano Lett. 19 (2019) 6800–6811.
[33] M. Daniyal, B. Liu, W. Wang, Curr. Med. Chem. 26 (2019) e120013.
[34] L. Zhang, L. Xu, Y. Wang, et al., Chin. Chem. Lett. 33 (2022) 4089–4095.
[35] J. Yan, Y. Zhang, L. Zheng, et al., Chin. Chem. Lett. 33 (2022) 767–772.
[36] Z.B. Yang, Y. Luo, Y.N. Hu, et al., Adv. Funct. Mater. 31 (2020) 2007991.
[37] H. Zhu, B. Zhang, N. Zhu, et al., Chin. Chem. Lett. 32 (2021) 1220–1223.
[38] Y. Li, R.B. Tang, X.Y. Liu, et al., ACS Nano 14 (2020) 16840–16853.
[39] Z.L. Zheng, Q. Chen, R. Dai, et al., Nanoscale 12 (2020) 11562–11572.
[40] Z. Liu, X. Yang, R. Liu, Bao, et al., Biomaterials 272 (2021) 120777.
[41] E. Okumus, E. Bakkalbasi, I. Javidipour, et al., Food Biosci. 42 (2021) 101158.
[42] E.E. Sweebey, J.C. Meijia, R. Fernandes, Small 14 (2018) 1800678.
[43] O. Kepp, L. Senovilla, I. Vitale, et al., Oncoimmunology 3 (2014) e955691.
[44] A. Showalter, A. Limaye, J.L. Oyer, et al., Cytokine 97 (2017) 123–132.
[45] C. Ji, J. Si, Y. Xu, et al., Theranostics 11 (2021) 8587–8604.